THE JOURNAL OF PHYSICAL CHEMISTRY C

Article

pubs.acs.org/JPCC

Mobile-Ion-Induced Degradation of Organic Hole-Selective Layers in Perovskite Solar Cells

Yicheng Zhao,[†,‡,§] Wenke Zhou,[†,§] Hairen Tan,[‡,§] Rui Fu,[†] Qi Li,[†,∥] Fang Lin,[†] Dapeng Yu,[†,⊥] Grant Walters,[‡] Edward H. Sargent,[*,‡] and Qing Zhao[*,†,⊥]

[†]State Key Laboratory for Mesoscopic Physics and Electron Microscopy Laboratory, School of Physics, Peking University, Beijing 100871, China

[‡]Department of Electrical and Computer Engineering, University of Toronto, 10 King's College Road, Toronto, Ontario M5S 3G4, Canada

[∥]UCLA-PKU Joint Research Institute in Science and Engineering and [⊥]Collaborative Innovation Center of Quantum Matter, Peking University, Beijing 100084, China

Supporting Information

ABSTRACT: Organometal halide perovskites are mixed electronic−ionic semiconductors. It is imperative to develop a deeper understanding of how ion-migration behavior in perovskites impacts the long-term operational stability of solar cells. In this work, we found that ion penetration from the perovskite layer into the adjacent organic hole-selective layer is a crucial cause of performance degradation in perovskite solar cells. The monovalent cation, namely, methylammonium (MA^+), is the main ion species that penetrates into the organic hole-selective layer of Spiro-MeOTAD because of the built-in electric field during operation. The incorporation of MA^+ induces deep-level defects in the Spiro-MeOTAD layer and thereby deteriorates the hole-transporting ability of Spiro-MeOTAD, degrading solar cell performance. Our work points to two ways to improve the stability of perovskite solar cells: one is to insert a compact ion-blocking layer between Spiro-MeOTAD and perovskite, and the other is to find a hole-selective layer that is insensitive to extraneous ions (MA^+).

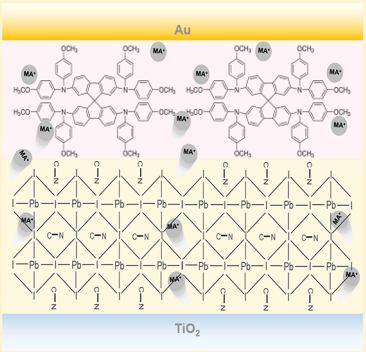

INTRODUCTION

Organometal halide perovskite solar cells require further progress to achieve long-term device stability. The decomposition of perovskite films due to moisture, oxygen, illumination, and other environmental factors has been explored and addressed in significant ways;[1−4] however, degradation of perovskite solar cells can still occur even without the decomposition of the perovskite absorber layer.[5−8] This suggests that the degradation of interfaces and charge-selective layers can also contribute to the fate of perovskite solar cells over time.

Ionic motion is a suspected cause of instability in perovskite-based devices because of the low energy barriers to ionic transport in organometal halide perovskites.[9−19] The activation energy for the migration of I, MA^+, and Pb^{2+} ions ranges from 0.1 to 1 eV.[10,13,19] Previous studies have shown that ion migration strongly influences the physicochemical properties of perovskite films by introducing deep-level defects,[14,20−22] doping effects, and polarization fields,[9,12,13,20] and that these effects can potentially cause gradual efficiency losses during device operation. Ion-migration-related degradation was also reported to be caused by redox reactions between metal contacts and iodide for silver and aluminum electrodes in both normal and inverted structures of perovskite solar cells.[23−26]

Although Al/Ag electrodes are not necessarily responsible for device degradation, it remains to be clarified whether and how ionic motion in perovskite films affects the charge-selective layers in perovskite solar cells with Au electrodes. The most common hole-selective layers (HSLs) in highly efficient perovskite solar cells consist of conjugated organic materials such as 2,2′,7,7′-tetrakis(*N*,*N*-di-4-methoxyphenylamino)-9,9′-spirobifluorene (Spiro-MeOTAD), poly(triarylamine) (PTAA), and their derivatives.[27−29] Hole transport depends on chemical doping and modification with trace additives such as lithium salts. Ion-migration behavior in perovskite polymorphs and consequent device degradation thus demands an understanding of how this behavior affects the organic HSL in perovskite solar cells, especially under device operating conditions.[30]

In this work, we found that over half of the efficiency loss in perovskite solar cells after operation originates from the degradation of the HSL. This performance loss can occur without any discernible perovskite decomposition. Through time-of-flight secondary-ion mass spectrometry (ToF-SIMS), we observed the evident penetration of methylammonium ions (MA^+) from the methylammonium lead iodide ($MAPbI_3$)

Received: May 15, 2017
Revised: June 25, 2017
Published: July 5, 2017

DOI: 10.1021/acs.jpcc.7b04684
J. Phys. Chem. C 2017, 121, 14517−14523

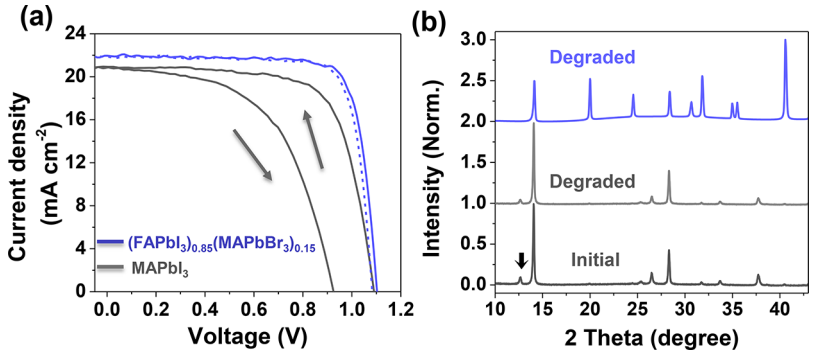

Figure 1. Current density−voltage (J−V) characterization of perovskite solar cells with different perovskite compositions: $MAPbI_3$ and $(MAPbBr_3)_{0.15}(FAPbI_3)_{0.85}$. (b) XRD patterns of $MAPbI_3$ (gray) and $(MAPbBr_3)_{0.15}(FAPbI_3)_{0.85}$ (purple) perovskite films in initial and degraded cells.

perovskite layer into the HSL. During device operation, the penetration of the organic cation can lead to increased deep-level defects and reduced doping concentrations in the HSL, leading to a loss of performance in devices.

METHODS

Device Fabrication. All chemicals were purchased from Sigma-Aldrich or J&K Scientific Ltd. unless otherwise stated. The photovoltaic devices were fabricated on fluorine-doped tin oxide (FTO) coated glass (Pilkington, Nippon Sheet Glass). First, laser-patterned FTO-coated glass substrates were cleaned in deionized water, acetone, and ethanol and then subjected to an ultraviolet treatment for 10 min. Then, a compact 30-nm TiO_2 layer was deposited on the FTO by spray pyrolysis at 450 °C from a precursor solution of titanium diisopropoxide bis(acetylacetonate) in anhydrous ethanol. After the spray coating, the substrates were left at 450 °C for 45 min and allowed to cool to room temperature. $MAPbI_3$ was prepared from methylammonium iodide (MAI)/lead acetate ($PbAc_2$) (Sigma-Aldrich) (3:1) precursor solution (215 and 172 mg mL^{-1} for MAI and $PbAc_2$, respectively) with an extra 4 μL of H_3PO_2 (Aladdin). Then, the solution was spin-coated onto the plasma-cleaned FTO/TiO_2 substrate. The film was sintered at 100 °C for 50 min in nitrogen ambient. The hole-selective layer was spin-coated onto the perovskite film at 3000 rpm for 40 s. The spin-coating formulation was prepared by dissolving 72.3 mg of 2,2′,7,7′-tetrakis(*N*,*N*-*p*-dimethoxyphenylamino)-9,9′-spirobifluorene (Spiro-MeOTAD), purchased from Yingkou OPV Tech New Energy Co. Ltd., 30 μL of 4-*tert*-butylpyridine (tBP), and 20 μL of a stock solution of 520 mg mL^{-1} lithium bis(trifluoromethylsulfonyl)imide (Li-TFSI) in acetonitrile in 1 mL of chlorobenzene. Finally, 90-nm-thick gold electrodes were deposited by thermal evaporation. The active area of the electrode was fixed at 16 mm^2.

For the lateral structure Au/perovskite/Au device, the well-established photoetching technique was used to prepare the 50-μm channel. After the evaporation of 150 nm of Au, these plates were immersed in acetone overnight and then washed with acetone and distilled water. Before spin-coating of the perovskite film, a 3-min oxygen plasma treatment was used to remove the residual organic material and decrease the defects on the surface of the plates.

Device Characterization. The current density−voltage (J−V) characteristics were obtained using an Agilent B2900 Series precision source/measure unit, and the cell was illuminated with a solar simulator (Solar IV-150A, Zolix) under AM1.5 irradiation (100 mW cm^{-2}). The light intensity was calibrated with a Newport calibrated KG5-filtered Si reference cell. We used a black mask to define the cell area, and the masking effect was confirmed by testing the short-circuit current (J_{sc}) with and without it, which gave a 5% J_{sc} difference. The J−V curves are measured from 1.5 to −0.2 V with a scan velocity 20 mV/s. The masked active area was 9 mm^2. For the steady-state efficiency measurements, the applied voltage was fixed at 0.7 V, and the current value was recorded every 0.1 s. After about 3 s, the current increased slowly when the light was turned on.

For XRD measurements, X-ray powder diagrams were recorded on an X'Pert MPD PRO instrument from PANalytical equipped with a ceramic tube (Cu anode, λ = 1.54060A), a secondary graphite (002) monochromator, and an RTMS X'Celerator detector and operated in Bragg−Brentano geometry. The samples were mounted without further modification, and the automatic divergence slit and beam mask were adjusted to the dimensions of the thin films. A step size of 0.008° was chosen, along with an acquisition time of up to 7.5 min/°. A baseline correction was applied to all X-ray powder diagrams to remove the broad diffraction peak arising from the amorphous glass slide.

The surface morphology of the perovskite thin film was characterized by scanning electron microscopy (SEM) (Nano430, FEI). The instrument used an electron beam accelerated at 15 kV.

Time-resolved fluorescence spectra were recorded with a high-resolution streak camera system (Hamamatsu C10910). We used an amplified mode-locked Ti:sapphire femtosecond laser system (Legend, Coherent) and a two-stage optical parametric amplifier (OperA Solo, Coherent) to generate the pump beam with a repetition rate of 1 kHz. All of the samples were excited at 517 nm at room temperature with a dose of ~110 nJ cm^{-2}. The top side of the perovskite layers (in contrast to the FTO side) was illuminated by the incident light.

ToF-SIMS measurements were made wit a time-of-flight secondary ion mass spectrometer (TOF.SIMS 5) from IONTOF company. Ar-ion clusters were used to bombard and etch the film; Bi ions were used to form negative or positive electrical segments.

The impedance spectrum was measured using a potentiostat/galvanostat (SP-150, Bio-Logic, Seyssinet-Pariset, France) at different biases. The FTO/TiO_2 side was the negative electrode for biases larger than 0 V, which was the same as for our current−voltage scan. The frequency was tuned from 0.1 Hz to

DOI: 10.1021/acs.jpcc.7b04684
J. Phys. Chem. C 2017, 121, 14517−14523

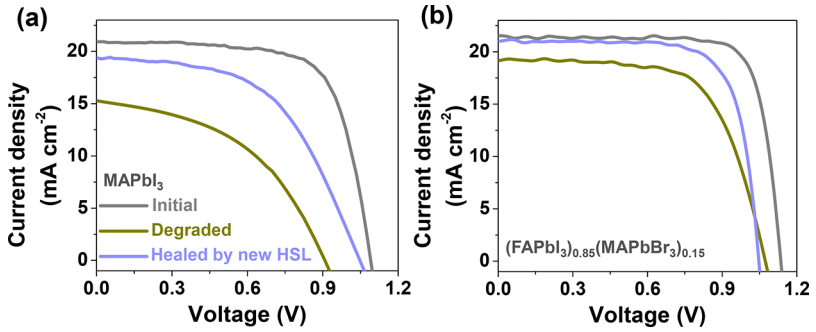

Figure 2. $J-V$ measurements of initial cells, degraded cells, and corresponding healed cells obtained by replacing the HSL in degraded cells for perovskite compositions of (a) $MAPbI_3$ and (b) $(FAPbI_3)_{0.85}(MAPbBr_3)_{0.15}$.

1 MHz with 70 data points, and at each point 200 measurements were averaged to smooth the impedance spectra. All samples were measured under 10 mW cm^{-2} using a 1/10 optical attenuator. The capacitance as a function of frequency was extracted using a resistor−capacitor (RC) circuit, and the eigen-relaxation time or recombination time can be obtained from either a Bode plot (frequency of the maximum phase angle) or a Nyquist plot (1/RC). The details of obtaining the trap density can be found in ref 34. For the identification of the energy levels of defects, we cited the conversion parameter between the applied frequency and energy level,[42] considering the same device architecture and contacting layer.

Galvanostatic standard measurements were performed using a potentiostat/galvanostat (SP-150, Bio-Logic, Seyssinet-Pariset, France) with a Au/$MAPbI_3$/Au structure. In the beginning of a cycle, the current value was preset at 20 nA, and then the current was switched off. The experiments are conducted in a nitrogen glovebox unless otherwise stated.

RESULTS AND DISCUSSION

We studied two types of perovskite solar cells both with the n-i-p planar architecture FTO/TiO_2/perovskite/Spiro-MeOTAD/Au. One type was a $MAPbI_3$ perovskite solar cell deposited on a high-temperature-sintered compact TiO_2 electron-selective layer (ESL); the other was a $(MAPbBr_3)_{0.15}(FAPbI_3)_{0.85}$ mixed perovskite solar cell with Cl-capped TiO_2 as the ESL.[31] As shown in Figure 1a, the $MAPbI_3$ device had a power conversion efficiency (PCE) of 16.1% under reverse scan and showed strong hysteresis. The $(MAPbBr_3)_{0.15}(FAPbI_3)_{0.85}$ device had a PCE of 19.9% without obvious hysteresis. Both devices exhibited performance degradation after working at the maximum power point under humid ambient conditions (Figure S1a,b). The faster degradation in air might be correlated with moisture-assisted $CH_3NH_3^+$ migration, demonstrated by Leijtens et al.[20] To examine whether the degradation was caused by perovskite decomposition, we measured X-ray diffraction (XRD) patterns of the perovskite films in the initial and degraded devices. Note that the Au and the HSL were removed before XRD measurements. No extra PbI_2 was observed in the degraded cells (Figure 1b), indicating negligible decomposition of the perovskite films.

Because TiO_2 and inert metallic Au should be stable, we posited that the vulnerable organic HSL (Spiro-MeOTAD in our devices) might degrade during solar cell operation. To verify this hypothesis, we replaced the Spiro-MeOTAD layer in the degraded devices with a fresh film, as illustrated in Figure S2. The corresponding $J-V$ curves and steady-state performance of the initial cells, degraded cells, and healed cells are shown in Figure 2a ($J-V$ for $MAPbI_3$), Figure2b [$J-V$ for $(MAPbBr_3)_{0.15}(FAPbI_3)_{0.85}$], Figure S3a (steady-state performance for $MAPbI_3$), Figure S3b [steady-state performance for$(MAPbBr_3)_{0.15}(FAPbI_3)_{0.85}$]. Table 1 provides a summary of the efficiencies for the same batch of devices at different stages (initial, degraded, and healed). The PCEs of the initial and degraded (after ∼8 min operating in air with ∼35% RH) $MAPbI_3$ cells were found to be 16.1% and 6.2%, respectively. The efficiency increased by 4.5% (absolute) after the replacement of the HSL. Performance recovery after replacement of the HSL was observed in the high-efficiency, hysteresis-free $(MAPbBr_3)_{0.15}(FAPbI_3)_{0.85}$ perovskite solar cells as well. Because the replaced HSLs were rougher, this process of Spiro-MeOTAD replacement would inevitably lead to a ∼1% absolute efficiency loss compared to devices without degradation (Table 1). The efficiency recovery indicates that at least half of the efficiency loss arose from the degradation of the HSL itself.

Table 1. Summary of the Power Conversion Efficiencies (PCEs) of the Same Batch of Devices at Different Stages (Initial, Degraded, and Healed)

	PCE (%)	
device	$MAPbI_3$	$FAPbI_3)_{0.85}(MAPbBr_3)_{0.15}$
initial	16.1 ± 1.5	18.9 ± 1.4
degraded (air)	4.9 ± 2.3	13.5 ± 2.4
healed by new HSL (air)	11.2 ± 1.9	15.7 ± 1.9
degraded (N_2)	6.5 ± 1.9	18.5 ± 1.6
healed by new HSL (N_2)	11.5 ± 1.6	17.8 ± 1.8

The HSL-related degradation rate was higher in $MAPbI_3$ devices than in $(FAPbI_3)_{0.85}(MAPbBr_3)_{0.15}$ devices, and it could also be increased by moisture, as shown in Table 1. To gain further insight into the degradation mechanism of the HSL, we used ToF-SIMS to examine the possibility of ion penetration from the perovskite film into the adjacent HSL. We sought, in this way, to analyze the chemical depth profile of fresh and degraded devices. First, by analyzing the ToF-SIMS spectra layer by layer (Figure S4), we confirmed that $CH_3NH_3^+$, Pb^+, and I_2^+ can well represent perovskite, whereas $C_7H_8O^+$ and Ti^+ represent HSL and TiO_2, respectively. The chemical depth profiles of ions through the fresh and degraded $MAPbI_3$ cells (Au/HSL/$MAPbI_3$/TiO_2) are shown in Figure 3a,b. Note that $C_7H_8O^+$ shows two peaks in the plot: the first peak corresponds to the HSL, and the second peak originates from perovskite, as shown in Figure S4. These results clearly show that the MA^+ has little overlap between the perovskite layer and the HSL in

DOI: 10.1021/acs.jpcc.7b04684
J. Phys. Chem. C 2017, 121, 14517−14523

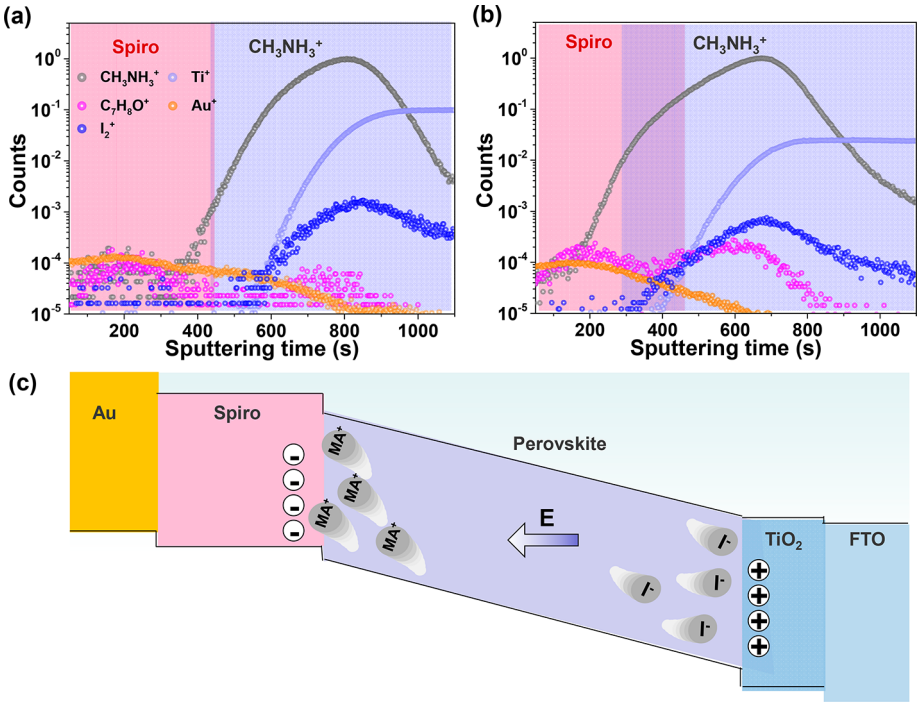

Figure 3. (a,b) Counts versus sputtering time for different ions in the Au/HSL/perovskite/TiO_2/FTO architecture in (a) fresh cells and (b) degraded devices with over 60% efficiency loss. (c) Schematic of the electric field distribution in perovskite solar cells and the corresponding direction of ion migration.

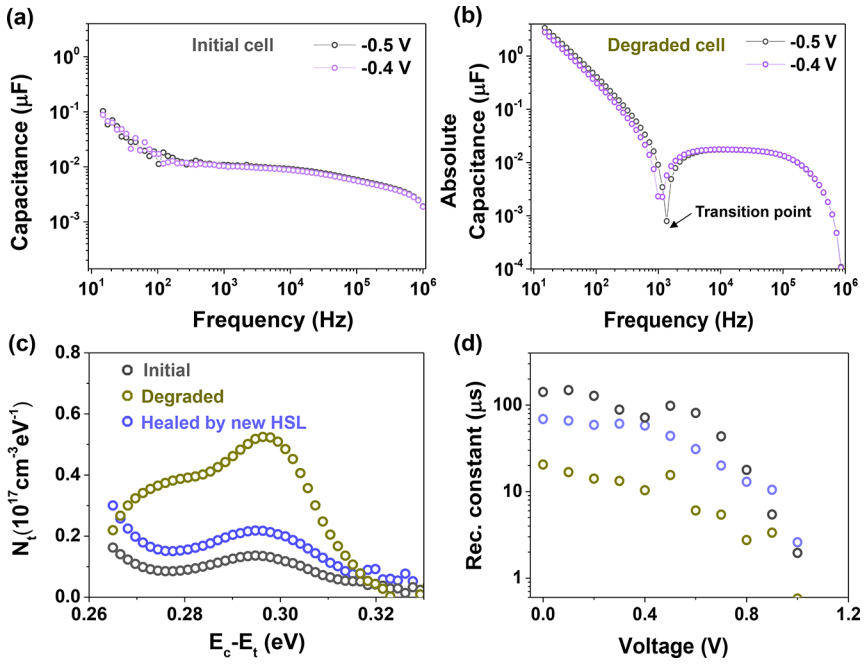

Figure 4. (a,b) Capacitance versus frequency in (a) fresh and (b) degraded cells. The arrow in panel b indicates the transition point where the capacitance value becomes negative at −0.4/−0.5 V bias. Note that we use absolute values in panel b and that the transition point indicates a value change from negative to positive. (c) Defect distributions in fresh, degraded, and healed cells. (d) Recombination time constants ($R_{rec}C_{rec}$) of fresh, degraded, and healed cells at different biases.

the fresh cells. However, in the degraded devices, there is an obvious overlap between the HSL and MA^+ distributions, especially close to the HSL/perovskite interface (purple area). Quantitative analysis of the distribution is presented in Figure S5 by means of a Gaussian fitting. This overlap clearly shows the penetration of MA^+ ions from the perovskite film into the Spiro-MeOTAD layer during solar cell operation. Meanwhile, the I^- distribution also shows an overlap with the HSL distribution in the degraded device. We also compared the signal of MA^+ (Figure S6a) and the HSL (Figure S6b) distribution together in the fresh and degraded cells. This comparison clearly demonstrates the striking difference in MA^+ distribution between the fresh and degraded cells (Figure S6c).

DOI: 10.1021/acs.jpcc.7b04684
J. Phys. Chem. C 2017, 121, 14517−14523

As illustrated in Figure 3c, the MA^+-ion penetration into the HSL can be explained by the ion motion with the electric field under illumination. Under the electric field, directed from the TiO_2 toward the HSL, MA^+ cations migrate from the perovskite into the HSL, whereas I^- tends to move toward the TiO_2. Here, we cannot exclude the possibility of I^- intrusion into the HSL because of the small overlap between the I^- distribution and the HSL in degraded cells. Compared to the MA^+ signal, the intensity of I^- counts was about 3 orders of magnitude lower. The small amount of I^- overlap with the HSL is not driven by the built-in electric field from the perovskite layer and might be related to the volatile nature of HI formation in the perovskite film under illumination and heating ($CH_3NH_3I \rightarrow CH_3NH_2$ + HI, and HI could enter the HSL). We did not observe an obvious difference in the gold distributions between the fresh and degraded devices (yellow circles in Figure 3a,b), indicating that gold migration was not involved in the irreversible degradation in our devices.[32]

To further reveal how MA^+-ion penetration deteriorates device performance, impedance spectra (IS) of $MAPbI_3$ solar cells at three stages (initial, degraded, and healed) were analyzed under 0.1-sun irradiation. IS is a well-established and widely used technique in dye-sensitized solar cells,[33] organic solar cells,[34] and perovskite solar cells.[35,36] Electronic parameters, such as capacitances and resistances in photovoltaic devices, can be decoupled by analyzing the frequency-dependent alternating-current response with appropriate equivalent circuits. Figure S7e shows the equivalent circuit used for our curve fitting, where the subscripts ext, rec, i, geo, and inter stand for external, recombination, internal, geometry, and interface, respectively. At the initial stage, the radius of the semicircle increases at a larger applied negative bias in the impedance plots of fresh cells (Figure S7b) and healed cells (Figure S7d), consistent with the presence of a widened space charge region. However, the degraded device presented the opposite tendency (Figure S7c). We also observed negative capacitance at −0.4/−0.5 V in the degraded cells below 1 kHz (Figure 4b), whereas the initial cells did not exhibit negative capacitance (Figure 4a), and the negative capacitance disappeared again in the healed cells (Figure S7a). Negative capacitance is closely related to sub-band-gap defects.[21,22,37−39]

Then, the density of defect states can be derived from the angular-frequency-dependent capacitance using the equation[40,41]

$$N_t(\omega) = -\left(\frac{V_{bi} - V_{app}}{qWkT}\right)\left(\frac{dC}{d\omega}\right)\omega \quad (1)$$

where V_{bi}, W, and V_{app} represent the built-in voltage, the width of the space charge region, and the applied voltage, respectively. The frequency ω can be converted into the energy level of defects (E_a) using the expression[42]

$$\omega = AT^2 \exp(-E_a/kT) \quad (2)$$

This equation can be interpreted in terms of the emission rate of carriers trapped by the defects at a specific energy level (Figure S8). Finally, one can obtain the defect energy distribution under different applied bias voltages as

$$N_t(E_a) = -\left(\frac{V_{bi} - V_{app}}{qWkT}\right)\left(\frac{dC}{df}\right)f \quad (3)$$

We compared the defect states as derived from the angular-frequency-dependent capacitance[43−48] (Figure 4c). Compared to its initial state, the degraded device had a much higher density of defects. After the HSL replacement (healed device), the density of defects dropped significantly again. Then, the related recombination time constant ($\tau_{rec} = R_{rec}C_{rec}$) can be extracted from this IS modeling. The recombination lifetimes of devices at various stages are shown in Figure 4d. Compared with the initial and healed devices, the degraded device had a much shorter recombination lifetime. The results here indicate that the MA^+-ion penetration mainly increased the defect density in the HSL and thus led to the degradation of solar cell performance as well.

In the high-frequency (∼1-MHz) region where only the bulk resistance of the perovskite and HSL dominates, we observed a 2-fold increase in resistivity in the degraded cells (from ∼3 to 7 Ω cm^2) (Figure S9a,b). The bulk resistance decreased after HSL replacement (Figure S9c). A change in resistance in the perovskite film was excluded by cyclic galvanostatic measurements (Figure S9d).[11,17,49] Considering that the TiO_2 and Au layers are robust, these sub-band-gap states and the increased resistivity should be caused by the degradation of the HSL. To demonstrate that MA^+ caused the detrimental destruction of Spiro-MeOTAD, we treated fresh devices with methylamine vapor for a very short period of time. Surprisingly, the efficiency dropped significantly even after 1 s of such vapor treatment (Figure S10b). Addition of 1 mg/mL MAI to Spiro-OMeTAD solution also resulted in poorly performing devices (Figure S10a). We found that the extent of device degradation resulting from excess MAI was greater than that resulting from a single MA vapor treatment. These results provide evidence that both MA^+ and I^- are detrimental to the Spiro-MeOTAD layer, and we could not exclude the possibility of I^- reducing the device performance in this work. However, Figure S10b provides strong evidence that MA^+ ion indeed play a role in destroying Spiro-MeOTAD. On the other hand, from the results of our ToF-SIMS experiments, MA^+ is the main species that migrates into the Spiro-MeOTAD layer. We summarize that the iodine-diffusion-induced performance degradation in $MAPbI_3$ and $(MAPbBr_3)_{0.15}(FAPbI_3)_{0.85}$ solar cells should be negligible. The detrimental effect of excess $CH_3NH_2^+$ or MA^+ on the Spiro-OMeTAD-based HSL might be related to a strong interaction of Spiro-MeOTAD with MA^+ because of the large dipole moment of MA^+,[50] similar to the situation with poly(3,4-ethylenedioxythiophene):poly(styrene sulfonate) (PEDOT:PSS).[51]

CONCLUSIONS

In summary, we have experimentally confirmed that ion penetration from the perovskite layer into the adjacent organic HSL is one of the key factors leading to the performance degradation of perovskite solar cells. The incorporation of MA^+ ions into the HSL causes energy disorder and reduced conductivity in the Spiro-OMeTAD layer, which results in rapid performance degradation for perovskite solar cells. Our work here highlights the need to find a new hole-selective layer that is insensitive to ion penetration or to insert an ion-blocking layer between the HSL and the perovskite to alleviate the efficiency loss during long-term operation.

DOI: 10.1021/acs.jpcc.7b04684
J. Phys. Chem. C 2017, 121, 14517−14523

■ ASSOCIATED CONTENT

Supporting Information

The Supporting Information is available free of charge on the ACS Publications website at DOI: 10.1021/acs.jpcc.7b04684.

Method details; steady-state output of the device; global mass spectra; impedance spectra of fresh, degraded, and healed devices; and galvanostatic data (DOCX)

■ AUTHOR INFORMATION

Corresponding Authors

*E-mail: ted.sargent@utoronto.ca.
*E-mail: zhaoqing@pku.edu.cn.

ORCID

Qing Zhao: 0000-0003-3374-6901

Author Contributions

§Y.Z., W.Z., and H.T. contributing equally to this work.

Notes

The authors declare no competing financial interest.

■ ACKNOWLEDGMENTS

This work was supported by National 973 Projects (2013CB932602, MOST) from the Ministry of Science and Technology, China, and the National Natural Science Foundation of China (NSFC 51622201, 61571015, 91433102, 11404009). H.T. acknowledges The Netherlands Organisation for Scientific Research (NWO) for a Rubicon grant (680-50-1511) in support of his postdoctoral research at University of Toronto.

■ REFERENCES

(1) Koushik, D.; Verhees, W. J. H.; Kuang, Y.; Veenstra, S.; Zhang, D.; Verheijen, M. A.; Creatore, M.; Schropp, R. E. I. High-efficiency humidity-stable planar perovskite solar cells based on atomic layer architecture. *Energy Environ. Sci.* **2017**, *10*, 91−100.

(2) Bai, Y.; Dong, Q.; Shao, Y.; Deng, Y.; Wang, Q.; Shen, L.; Wang, D.; Wei, W.; Huang, J. Enhancing stability and efficiency of perovskite solar cells with crosslinkable silane-functionalized and doped fullerene. *Nat. Commun.* **2016**, *7*, 12806.

(3) Zhao, Y.; Wei, J.; Li, H.; Yan, Y.; Zhou, W.; Yu, D.; Zhao, Q. A polymer scaffold for self-healing perovskite solar cells. *Nat. Commun.* **2016**, *7*, 10228.

(4) Aristidou, N.; Sanchez-Molina, I.; Chotchuangchutchaval, T.; Brown, M.; Martinez, L.; Rath, T.; Haque, S. A. The role of oxygen in the degradation of methylammonium lead trihalide perovskite photoactive layers. *Angew. Chem., Int. Ed.* **2015**, *54*, 8208−12.

(5) Guerrero, A.; You, J.; Aranda, C.; Kang, Y. S.; Garcia-Belmonte, G.; Zhou, H.; Bisquert, J.; Yang, Y. Interfacial degradation of planar lead halide perovskite solar cells. *ACS Nano* **2016**, *10*, 218−24.

(6) Zhao, L.; Kerner, R. A.; Xiao, Z.; Lin, Y. L.; Lee, K. M.; Schwartz, J.; Rand, B. P. Redox chemistry dominates the degradation and decomposition of metal halide perovskite optoelectronic devices. *ACS Energy Lett.* **2016**, *1*, 595−602.

(7) Berhe, T. A.; Su, W.-N.; Chen, C.-H.; Pan, C.-J.; Cheng, J.-H.; Chen, H.-M.; Tsai, M.-C.; Chen, L.-Y.; Dubale, A. A.; Hwang, B.-J. Organometal halide perovskite solar cells: degradation and stability. *Energy Environ. Sci.* **2016**, *9*, 323−56.

(8) Nie, W.; Blancon, J. C.; Neukirch, A. J.; Appavoo, K.; Tsai, H.; Chhowalla, M.; Alam, M. A.; Sfeir, M. Y.; Katan, C.; Even, J.; et al. Light-activated photocurrent degradation and self-healing in perovskite solar cells. *Nat. Commun.* **2016**, *7*, 11574.

(9) Xiao, Z.; Yuan, Y.; Shao, Y.; Wang, Q.; Dong, Q.; Bi, C.; Sharma, P.; Gruverman, A.; Huang, J. Giant switchable photovoltaic effect in organometal trihalide perovskite devices. *Nat. Mater.* **2014**, *14*, 193−198.

(10) Brenner, T. M.; Egger, D. A.; Kronik, L.; Hodes, G.; Cahen, D. Hybrid organic—inorganic perovskites: low-cost semiconductors with intriguing charge-transport properties. *Nat. Rev. Mater.* **2016**, *1*, 15007.

(11) Mizusaki, J.; Arai, K.; Fueki, K. Ionic conduction of the perovskite-type halides. *Solid State Ionics* **1983**, *11*, 203−211.

(12) Meloni, S.; Moehl, T.; Tress, W.; Franckevicius, M.; Saliba, M.; Lee, Y. H.; Gao, P.; Nazeeruddin, M. K.; Zakeeruddin, S. M.; Rothlisberger, U.; et al. Ionic polarization-induced current−voltage hysteresis in $CH_3NH_3PbX_3$ perovskite solar cells. *Nat. Commun.* **2016**, *7*, 10334.

(13) Eames, C.; Frost, J. M.; Barnes, P. R.; O'Regan, B. C.; Walsh, A.; Islam, M. S. Ionic transport in hybrid lead iodide perovskite solar cells. *Nat. Commun.* **2015**, *6*, 7497.

(14) Zhao, Y.; Zhou, W.; Ma, W.; Meng, S.; Li, H.; Wei, J.; Fu, R.; Liu, K.; Yu, D.; Zhao, Q. Correlations between immobilizing ions and suppressing hysteresis in perovskite solar cells. *ACS Energy Lett.* **2016**, *1*, 266−272.

(15) Leijtens, T.; Eperon, G. E.; Noel, N. K.; Habisreutinger, S. N.; Petrozza, A.; Snaith, H. J. Stability of metal halide perovskite solar cells. *Adv. Energy Mater.* **2015**, *5*, 1500963.

(16) Yuan, Y.; Wang, Q.; Shao, Y.; Lu, H.; Li, T.; Gruverman, A.; Huang, J. Electric-field-driven reversible conversion between methylammonium lead triiodide perovskites and lead iodide at elevated temperatures. *Adv. Energy Mater.* **2016**, *6*, 1501803.

(17) Yang, T.; Gregori, G.; Pellet, N.; Gratzel, M.; Maier, J. The significance of ion conduction in a hybrid organic-inorganic lead-iodide-based perovskite photosensitizer. *Angew. Chem., Int. Ed.* **2015**, *54*, 7905−7910.

(18) Hoke, E. T.; Slotcavage, D. J.; Dohner, E. R.; Bowring, A. R.; Karunadasa, H. I.; McGehee, M. D. Reversible photo-induced trap formation in mixed-halide hybrid perovskites for photovoltaics. *Chem. Sci.* **2015**, *6*, 613−617.

(19) Zhao, Y.-C.; Zhou, W.-K.; Zhou, X.; Liu, K.-H.; Yu, D.-P.; Zhao, Q. Quantification of light-enhanced ionic transport in lead iodide perovskite thin films and its solar cell applications. *Light: Sci. Appl.* **2017**, *6*, e16243.

(20) Leijtens, T.; Hoke, E. T.; Grancini, G.; Slotcavage, D. J.; Eperon, G. E.; Ball, J. M.; De Bastiani, M.; Bowring, A. R.; Martino, N.; Wojciechowski, K.; McGehee, M. D.; Snaith, H. J.; Petrozza, A. Mapping electric field-induced switchable poling and structural degradation in hybrid lead halide perovskite thin films. *Adv. Energy Mater.* **2015**, *5*, 1500962.

(21) Zhang, Y.; Liu, M.; Eperon, G. E.; Leijtens, T. C.; McMeekin, D.; Saliba, M.; Zhang, W.; de Bastiani, M.; Petrozza, A.; Herz, L. M.; Johnston, M. B.; Lin, H.; Snaith, H. J. Charge selective contacts, mobile ions and anomalous hysteresis in organic−inorganic perovskite solar cells. *Mater. Horiz.* **2015**, *2*, 315−322.

(22) Leijtens, T.; Srimath Kandada, A. R.; Eperon, G. E.; Grancini, G.; D'Innocenzo, V.; Ball, J. M.; Stranks, S. D.; Snaith, H. J.; Petrozza, A. Modulating the electron−hole interaction in a hybrid lead halide perovskite with an electric field. *J. Am. Chem. Soc.* **2015**, *137*, 15451−15459.

(23) Kato, Y.; Ono, L. K.; Lee, M. V.; Wang, S.; Raga, S. R.; Qi, Y. Silver iodide formation in methylammonium lead iodide perovskite solar cells with silver top electrodes. *Adv. Mater. Interfaces* **2015**, *2*, 1500195.

(24) Zhang, T.; Meng, X.; Bai, Y.; Xiao, S.; Hu, C.; Yang, Y.; Chen, H.; Yang, S. Profiling the organic cation-dependent degradation of organolead halide perovskite solar cells. *J. Mater. Chem. A* **2017**, *5*, 1103−1111.

(25) Matteocci, F.; Busby, Y.; Pireaux, J.-J.; Divitini, G.; Cacovich, S.; Ducati, C.; Di Carlo, A. Interface and composition analysis on perovskite solar cells. *ACS Appl. Mater. Interfaces* **2015**, *7*, 26176−26183.

(26) Misra, R. K.; Ciammaruchi, L.; Aharon, S.; Mogilyansky, D.; Etgar, L.; Visoly-Fisher, I.; Katz, E. A. Effect of halide composition on the photochemical stability of perovskite photovoltaic materials. *ChemSusChem* **2016**, *9*, 2572−2577.

DOI: 10.1021/acs.jpcc.7b04684
J. Phys. Chem. C 2017, 121, 14517−14523

(27) Rakstys, K.; Abate, A.; Dar, M. I.; Gao, P.; Jankauskas, V.; Jacopin, G.; Kamarauskas, E.; Kazim, S.; Ahmad, S.; Gratzel, M.; et al. Triazatruxene-based hole transporting materials for highly efficient perovskite solar cells. *J. Am. Chem. Soc.* **2015**, *137*, 16172−16178.
(28) Ameen, S.; Rub, M. A.; Kosa, S. A.; Alamry, K. A.; Akhtar, M. S.; Shin, H. S.; Seo, H. K.; Asiri, A. M.; Nazeeruddin, M. K. Perovskite solar cells: Influence of hole transporting materials on power conversion efficiency. *ChemSusChem* **2016**, *9*, 10−27.
(29) Wang, Y.; Yuan, Z.; Shi, G.; Li, Y.; Li, Q.; Hui, F.; Sun, B.; Jiang, Z.; Liao, L. Dopant-free Spiro-triphenylamine/fluorene as hole-transporting material for perovskite solar cells with enhanced efficiency and stability. *Adv. Funct. Mater.* **2016**, *26*, 1375−1381.
(30) Carrillo, J.; Guerrero, A.; Rahimnejad, S.; Almora, O.; Zarazua, I.; Mas-Marza, E.; Bisquert, J.; Garcia-Belmonte, G. Ionic reactivity at contacts and aging of methylammonium lead triiodide perovskite solar cells. *Adv. Energy Mater.* **2016**, *6*, 1502246.
(31) Tan, H.; Jain, A.; Voznyy, O.; Lan, X.; García de Arquer, F.; Fan, J. Z.; Quintero-Bermudez, R.; Yuan, M.; Zhang, B.; Zhao, Y.; et al. Efficient and stable solution-processed planar perovskite solar cells via contact passivation. *Science* **2017**, *355*, 722−726.
(32) Domanski, K.; Correa-Baena, J. P.; Mine, N.; Nazeeruddin, M. K.; Abate, A.; Saliba, M.; Tress, W.; Hagfeldt, A.; Gratzel, M. Not all that glitters is gold: metal-migration-induced degradation in perovskite solar ells. *ACS Nano* **2016**, *10*, 6306−6314.
(33) Bisquert, J.; Fabregat-Santiago, F.; Mora-Sero, I.; Garcia-Belmonte, G.; Gimenez, S. Electron lifetime in dye-sensitized solar cells: theory and interpretation of measurements. *J. Phys. Chem. C* **2009**, *113*, 17278−17290.
(34) Fabregat-Santiago, F.; Garcia-Belmonte, G.; Mora-Sero, I.; Bisquert, J. Characterization of nanostructured hybrid and organic solar cells by impedance spectroscopy. *Phys. Chem. Chem. Phys.* **2011**, *13*, 9083−9118.
(35) Kim, H.-S.; Mora-Sero, I.; Gonzalez-Pedro, V.; Fabregat-Santiago, F.; Juarez-Perez, E. J.; Park, N.-G.; Bisquert, J. Mechanism of carrier accumulation in perovskite thin-absorber solar cells. *Nat. Commun.* **2013**, *4*, 2242.
(36) Dualeh, A.; Moehl, T.; Tetreault, N.; Teuscher, J.; Gao, P.; Nazeeruddin, M. K.; Graetzel, M. Impedance spectroscopic analysis of lead iodide perovskite-sensitized solid-state solar cells. *ACS Nano* **2014**, *8*, 4053−4053.
(37) Wang, X.; Cai, C. A possible mechanism for the negative capacitance observed in organic devices. 2012. arXiv:1210.7904. arXiv.org e-Print archive. https://arxiv.org/abs/1210.7904.
(38) Mora-Sero, I.; Bisquert, J.; Fabregat-Santiago, F.; Garcia-Belmonte, G.; Zoppi, G.; Durose, K.; Proskuryakov, Y.; Oja, I.; Belaidi, A.; Dittrich, T.; Tena-Zaera, R.; Katty, A.; Lévy-Clément, C.; Barrioz, V.; Irvine, S. J. C. Implications of the negative capacitance observed at forward bias in nanocomposite and polycrystalline solar cells. *Nano Lett.* **2006**, *6*, 640−650.
(39) Bansal, K.; Datta, S. Voltage modulated electro-luminescence spectroscopy to understand negative capacitance and the role of sub-bandgap states in light emitting devices. *J. Appl. Phys.* **2011**, *110*, 114509.
(40) Herberholz, R.; Igalson, M.; Schock, H. W. Distinction between bulk and interface states in $CuInSe_2$/CdS/ZnO by space charge spectroscopy. *J. Appl. Phys.* **1998**, *83*, 318−325.
(41) Walter, T.; Herberholz, R.; Müller, C.; Schock, H. W. Determination of defect distributions from admittance measurements and application to Cu(In,Ga)Se_2 based heterojunctions. *J. Appl. Phys.* **1996**, *80*, 4411−4420.
(42) Duan, H.-S.; Zhou, H.; Chen, Q.; Sun, P.; Luo, S.; Song, T.-B.; Bob, B.; Yang, Y. The identification and characterization of defect states in hybrid organic-inorganic perovskite photovoltaics. *Phys. Chem. Chem. Phys.* **2015**, *17*, 112−116.
(43) Ehrenfreund, E.; Lungenschmied, C.; Dennler, G.; Neugebauer, H.; Sariciftci, N. S. Negative capacitance in organic semiconductor devices: Bipolar injection and charge recombination mechanism. *Appl. Phys. Lett.* **2007**, *91*, 012112.
(44) Pockett, A.; Eperon, G. E.; Peltola, T.; Snaith, H. J.; Walker, A.; Peter, L. M.; Cameron, P. J. Characterization of planar lead halide perovskite solar cells by impedance spectroscopy, open-circuit photovoltage decay, and intensity-modulated photovoltage/photocurrent spectroscopy. *J. Phys. Chem. C* **2015**, *119*, 3456−3465.
(45) Fabregat-Santiago, F.; Garcia-Belmonte, G.; Mora-Sero, I.; Bisquert, J. Characterization of nanostructured hybrid and organic solar cells by impedance spectroscopy. *Phys. Chem. Chem. Phys.* **2011**, *13*, 9083−9118.
(46) Shao, Y.; Xiao, Z.; Bi, C.; Yuan, Y.; Huang, J. Origin and elimination of photocurrent hysteresis by fullerene passivation in $CH_3NH_3PbI_3$ planar heterojunction solar cells. *Nat. Commun.* **2014**, *5*, 5784.
(47) Shao, Y.; Wang, Q.; Dong, Q.; Yuan, Y.; Huang, J. Vacuum-free laminated top electrode with conductive tapes for scalable manufacturing of efficient perovskite solar cells. *Nano Energy* **2015**, *16*, 47−53.
(48) Zhou, W.; Zhao, Y.; Shi, C.; Huang, H.; Wei, J.; Fu, R.; Liu, K.; Yu, D.; Zhao, Q. Reversible healing effect of water molecules on fully crystallized metal−halide perovskite film. *J. Phys. Chem. C* **2016**, *120*, 4759−4765.
(49) Yokota, I. On the electrical conductivity of cuprous sulfide: A diffusion theory. *J. Phys. Soc. Jpn.* **1953**, *8*, 595−602.
(50) Frost, J. M.; Butler, K. T.; Brivio, F.; Hendon, C. H.; van Schilfgaarde, M.; Walsh, A. Atomistic origins of high-performance in hybrid halide perovskite solar cells. *Nano Lett.* **2014**, *14*, 2584−2590.
(51) Liu, T.; Jiang, F.; Tong, J.; Qin, F.; Meng, W.; Jiang, Y.; Li, Z.; Zhou, Y. Reduction and oxidation of poly(3,4-ethylenedioxythiophene):poly(styrenesulfonate) induced by methylamine (CH_3NH_2)-containing atmosphere for perovskite solar cells. *J. Mater. Chem. A* **2016**, *4*, 4305−4311.

DOI: 10.1021/acs.jpcc.7b04684
J. Phys. Chem. C 2017, 121, 14517−14523